DISCLAIMER

This report was prepared as an account of work sponsored by an agency of the United States Government. Neither the United States Government nor any agency thereof, nor any of their employees, makes any warranty, express or implied, or assumes any legal liability or responsibility for the accuracy, completeness, or usefulness of any information, apparatus, product, or process disclosed, or represents that its use would not infringe privately owned rights. Reference herein to any specific commercial product, process, or service by trade name, trademark, manufacturer, or otherwise does not necessarily constitute or imply its endorsement, recommendation, or favoring by the United States Government or any agency thereof. The views and opinions of authors expressed herein do not necessarily state or reflect those of the United States Government or any agency thereof. Reference herein to any social initiative (including but not limited to Diversity, Equity, and Inclusion (DEI); Community Benefits Plans (CBP); Justice 40; etc.) is made by the Author independent of any current requirement by the United States Government and does not constitute or imply endorsement, recommendation, or support by the United States Government or any agency thereof.

ORNL/SPR-2025/3773

Low-Dose Neutron Irradiation Effects on Mechanical Properties of Additively Manufactured SS-316

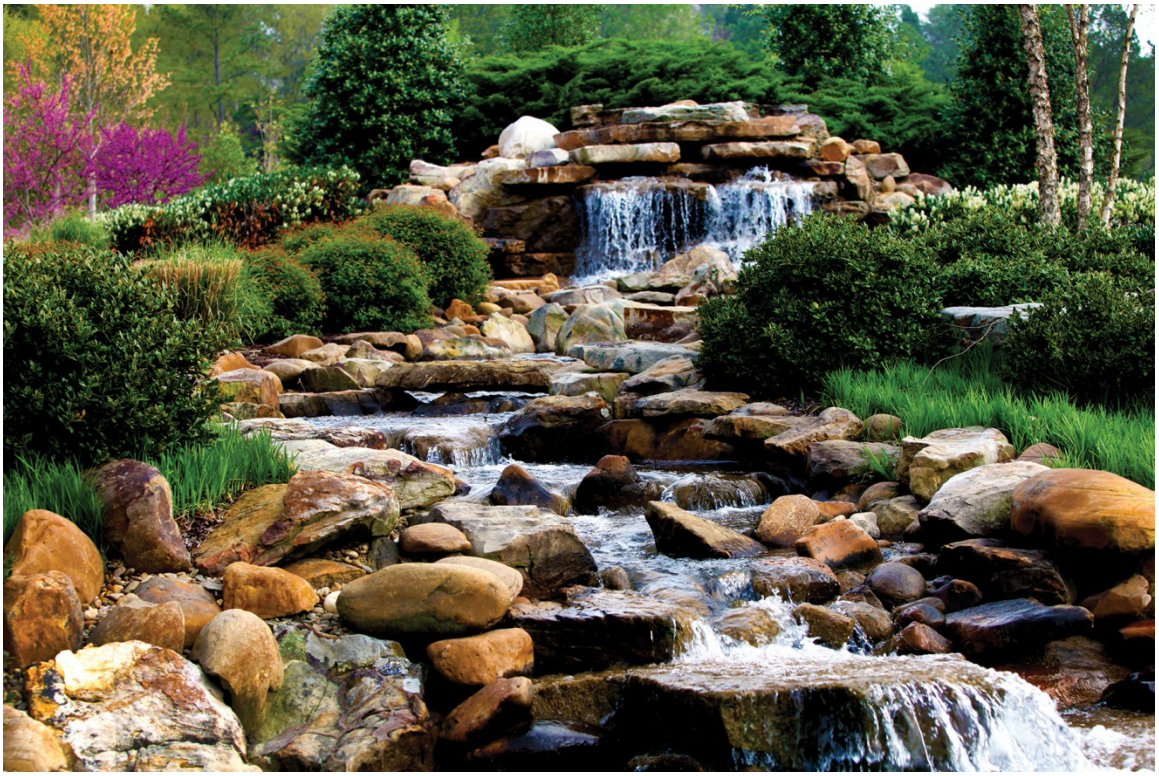

Caleb Massey
Annabelle Le Coq
Jesse Werden
David Collins
Anthony Guajardo
TS Byun
Patrick Champlin
Nick Russell
Kory Linton

Approved for public release.
Distribution is unlimited

March 2025

M3CR-22OR0404023

OAK RIDGE National Laboratory

ORNL IS MANAGED BY UT-BATTELLE LLC FOR THE US DEPARTMENT OF ENERGY

ORNL/SPR-2025/3773

Advanced Materials and Manufacturing Technologies Program

LOW-DOSE NEUTRON IRRADIATION EFFECTS ON MECHANICAL PROPERTIES OF ADDITIVELY MANUFACTURED SS-316

Caleb Massey
Annabelle Le Coq
Jesse Werden
David Collins
Anthony Guajardo
TS Byun
Patrick Champlin
Nick Russell
Kory Linton

March 2025

M3CR-22OR0404023

Prepared by
OAK RIDGE NATIONAL LABORATORY
Oak Ridge, TN 37831
managed by
UT-BATTELLE LLC
for the
US DEPARTMENT OF ENERGY
under contract DE-AC05-00OR22725

CONTENTS

FIGURES

TABLES

ABBREVIATIONS AND ACRONYMS

A709	Alloy 709
AM	additive manufacturing
AMMT	Advanced Materials and Manufacturing Technologies
BD	build direction
DED	direct energy deposition
GENTEN	general tensile
HFIR	High Flux Isotope Reactor
IMET	Irradiated Materials Examination and Testing
LAMDA	Low Activation Materials Development and Analysis
LPBF	laser powder bed fusion
MBS	miniature bend bar slotted
MINBEN	miniature bend bar
ORNL	Oak Ridge National Laboratory
PH	precipitation-hardened
PIE	postirradiation examination
SA	solution-annealed
SiC	silicon carbide
SR	stress-relieved
SS	stainless steel
TE	total elongation
TD	transverse direction
UE	uniform elongation
UTS	ultimate tensile strength
VED	volumetric energy density
YS	yield strength

SUMMARY

As part of an effort to qualify laser powder bed fusion (LPBF) SS-316H material for use in advanced reactors, the US Department of Energy Office of Nuclear Energy's Advanced Materials and Manufacturing Technologies (AMMT) program recently initiated a three-phase irradiation campaign on LPBF SS-316H to assess modes of material degradation at elevated temperatures (400–600°C) to irradiation doses up to 10 dpa. The first of three irradiations—conducted in the High Flux Isotope Reactor (HFIR) at Oak Ridge National Laboratory—assessed the level of degradation of one heat of LPBF SS-316H material produced using at least two different representative processing parameters and post-build heat treatments in comparison with reference wrought material. In FY 2023, 20 irradiation vehicles comprising 240 test specimens were inserted in HFIR, and post-irradiation examination was recently completed on the lower-dose (2 dpa) specimens.

Following sample disassembly and inventory, measurements of SiC thermometry specimens indicated that the irradiation was successful at reaching the target irradiation temperature within 16%. At least one rabbit in each condition successfully reached within 20°C of the target irradiation temperature. At least one irradiation capsule deviated from the target irradiation temperature of 600°C by approximately 88°C. Therefore, the test matrix was altered to include testing at 400°C, 500°C, and 600°C to provide fewer statistics but a larger breadth of test conditions to elucidate temperature-dependent performance vs. unirradiated conditions.

Tensile testing of the LPBF SS-316H specimens revealed no significant change in ductility for stress-relieved specimens when these specimens were tested at elevated temperatures following irradiation, although significant ductility loss was noted for solution-annealed LPBF SS-316H specimens at all irradiation conditions. The stress-relieved and solution-annealed LPBF SS-316H showed similar postirradiation ductility. No significant changes in postirradiation strength or ductility were noted for wrought SS-316H, except for marginal increases in yield strength at an irradiation temperature of approximately 400°C. Conversely, the ductility of the advanced wrought Alloy 709 decreased following all irradiation conditions to a level close to that of the stress-relieved SS-316H.

In addition to changes in ductility following irradiation, room temperature investigations of LPBF and wrought SS-316H revealed differential levels of fracture toughness change following irradiation. For the wrought SS-316H material, fracture toughness decreased by approximately 30%, whereas for the LPBF SS-316H material, fracture toughness only showed marginal changes vs. unirradiated measured values. Even with the drastic decrease in wrought SS-316H fracture toughness, the wrought material retained higher fracture toughness than any of the LPBF SS-316H material conditions, regardless of postbuild heat treatment or specimen orientation.

1. INTRODUCTION

In an effort to promote accelerated qualification of advanced reactor concepts, the US Department of Energy Office of Nuclear Energy's Advanced Materials and Manufacturing Technologies (AMMT) program is funding a multifaceted effort to increase the number of materials qualified for elevated temperature use (>400°C) in advanced nuclear reactors. This effort has included code case development for SS-316H produced via laser powder bed fusion (LPBF). The challenges related to LPBF stem from variability in microstructure and material properties that can be a result of the powder feedstock [1], the process parameters [2], the geometry [3], or the additive manufacturing (AM) system used [4]. The intrinsic heterogeneity in LPBF components makes current qualification initiatives impractical because fundamental assumptions regarding sampling material, grain structure, and chemical distributions, among other factors, are not translatable between wrought and additively manufactured components.

As part of the program's efforts to develop a processing envelope for LPBF SS-316H, multiple sets of processing parameters were identified using a General Electric (GE) Concept Laser M2 system. The use of this system resulted in LPBF SS-316H material with high strength, suitable ductility, and minimal levels of preferred grain orientation [5]. Two of these build parameters were later scaled into larger plates for the evaluation of high-temperature tensile and creep performance within the program [6]. These builds, labeled as Tensile Blocks 01 and Tensile Blocks 02 in previous reports [5, 6], were printed with parameters equating to equivalent volumetric energy densities (VEDs) of 71 J/mm^3 and 52 J/mm^3, respectively, using powder printed from a representative batch of SS-316H feedstock (Praxair Lot 3 powder with a carbon content of 0.08 wt % carbon). The strength, dislocation substructures, and grain morphology/textures of these two materials were noted to be similar, but the as-printed porosity was fundamentally different between the two builds (0.003% for Tensile Blocks 01 and 0.3% for Tensile Blocks 02). It was determined that the creep resistance of these two builds, albeit with only small changes in processing parameters, resulted in a significant difference of creep rupture life between the two builds (by a factor of 2×) [6].

Because of the intrinsic heterogeneity that may exist in LPBF components owing to changes in solidification rate as a function of part chemistry or printing geometry, microstructures representing both sets of processing parameters discussed above may be able to coexist within a printed component. Therefore, assessing whether postirradiation mechanical property degradation is linked to minor changes in as-built porosity or other microstructural features within optimized printing parameter ranges is of interest. For this reason, an initial irradiation campaign was performed at the High Flux Isotope Reactor (HFIR) at Oak Ridge National Laboratory (ORNL). This campaign was designed to compare the time-independent property degradation of the two different LPBF SS-316H builds mentioned herein (with two representative postbuild heat treatments and test orientations) with the property degradation of wrought SS-316H, advanced wrought Alloy 709 (A709), and other relevant SS-316L material produced via direct energy deposition (DED).

This work summarizes the status of the first HFIR irradiation (titled HFIR-1 in planning documentation) and presents the postirradiation examination mechanical test data generated to date within the HFIR-1 irradiation campaign on the LPBF and wrought materials.

2. HFIR IRRADIATION OVERVIEW

2.1 CAPSULE IRRADIATION DESIGNS

Two different types of HFIR capsules were used in this SS-316H irradiation campaign: the general tensile (GENTEN) capsule design [7] and the miniature bend bar (MINBEN) capsule design [8]. These capsule designs accommodate small mechanical testing specimens (either tensile specimens or fracture toughness specimens). A GENTEN capsule can hold 24 SS-J3 tensile specimens (0.75 mm thick). The specimens are stacked in quadrants in each of the three aluminum or molybdenum holders and pressed onto the holders' inner wall via central spring pins. Chevrons are added on each side of the specimen gauge stacks for heat transfer purposes. Silicon carbide passive thermometry is placed in each quadrant of each holder. Each holder assembly is referred to as "tier". Figure 1 illustrates the GENTEN capsule design. The MINBEN design (shown in Figure 2) accommodates a total of six MBS-1 (miniature bend bar slotted) specimens held within a single aluminum or molybdenum holder. Three MBS-1 specimens are axially stacked on the opposite side of the holder and pressed onto the inner walls of the holder using SiC springs. Long SiC thermometry is located on the top and the bottom of each stack of specimens. For both GENTEN and MINBEN designs, springs are inserted at the top and bottom of the housing to ensure the holder(s) stay(s) centered within the housing. The combination of holder material, holder OD (which dictates the size of the capsule gas gap), fill gas mixture, and axial position in HFIR's flux trap leads to the desired target temperature.

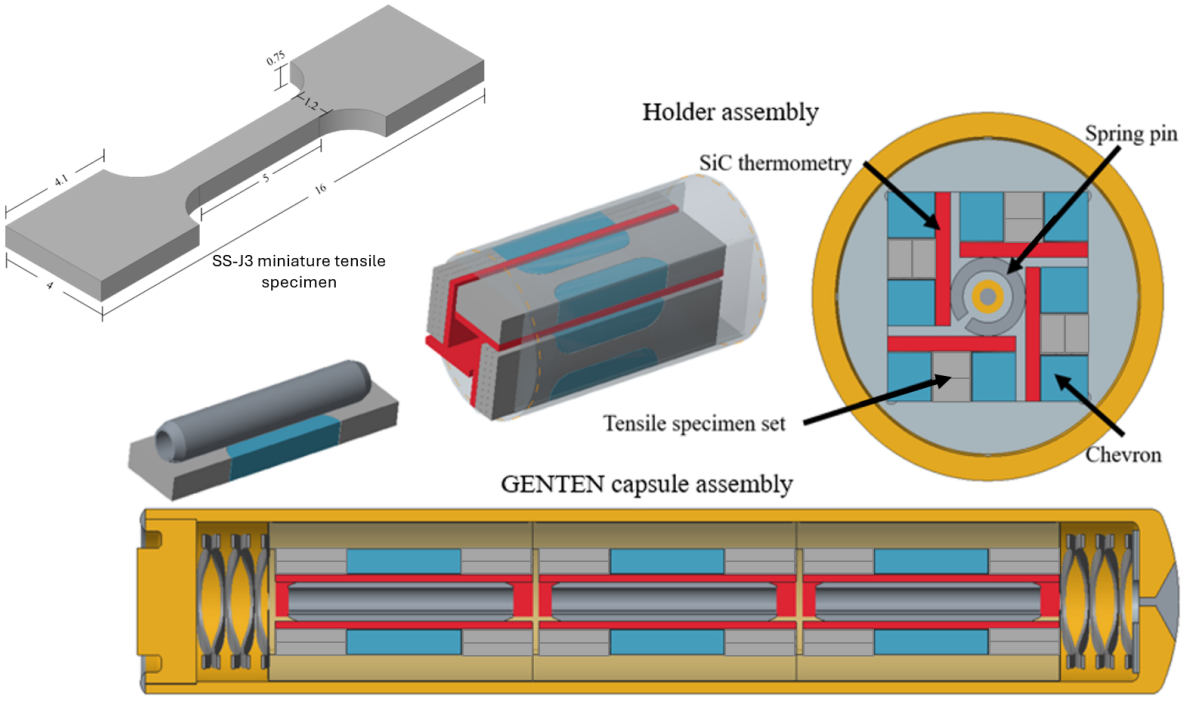

Figure 1. GENTEN capsule design accommodating 24 SS-J3 specimens.

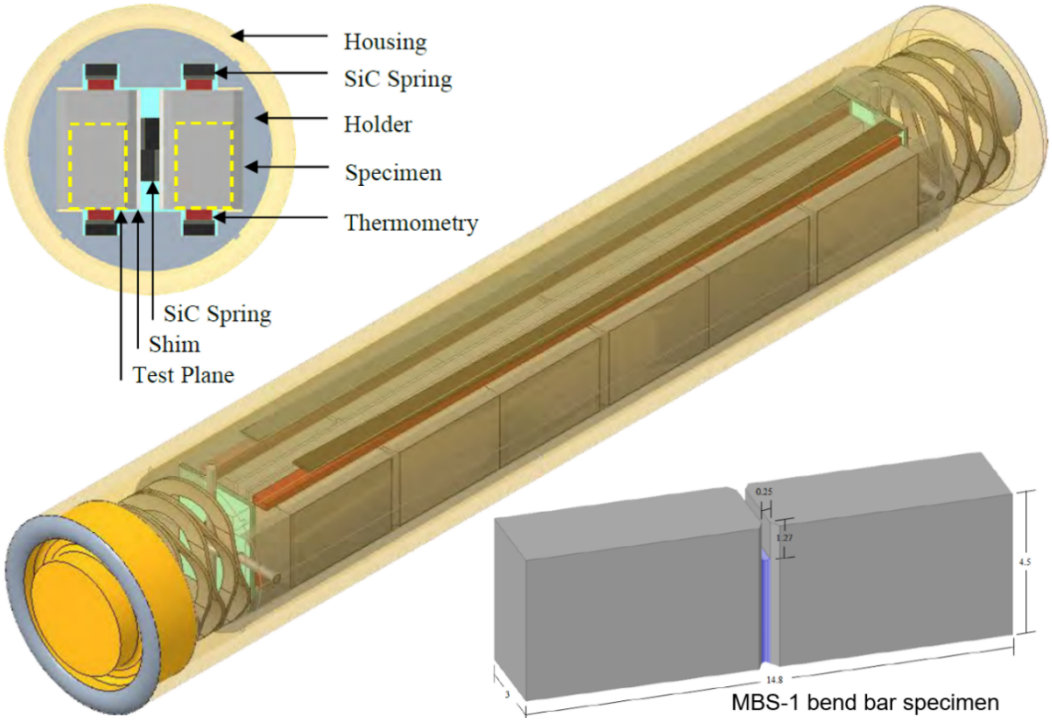

Figure 2. MINBEN capsule design accommodating six MBS-1 specimens.

2.2 IRRADIATION TEST MATRIX

Details of the irradiation test matrix are available in Champlin et al. [8]. In summary, the irradiation test matrix was developed in line with the Nuclear Energy Agency report on structural materials for advanced nuclear systems [9] with the objective of generating data comparable to existing AM 316L neutron-irradiated data. Two different target irradiation temperatures were chosen: (1) 400°C to study irradiation-induced segregation phase stability, as well as the potential hardening or softening behavior of the material, and (2) 600°C to study softening and microstructural stability.

Specimens were fabricated from SS-316H blocks fabricated using an LPBF process with two different energy depositions. For each energy deposition, material in stress-relieved (24 h at 650°C, SR) and solution-annealed (1 h at 1100°C, SA) conditions was produced. Specimens were harvested from the AM builds in both the build direction (BD) and the transverse direction (TD) to reveal any anisotropy in crack propagation or tensile properties. In addition to AM 316H SS specimens, specimens were also machined from AM SS-316L built by DED and in stress-relieved condition, as well as wrought austenitic steels (316H and A709). For a relevant comparison, the wrought SS-316H was solution-annealed at the same conditions as the LPBF SS-316H parts. However, A709 (ATI heat number 529900) was irradiated in the precipitation-hardened (10 h at 775°C, PH) condition.

The irradiation test matrix comprises 20 irradiation capsules: 8 GENTEN capsules (GAMT1 to GAMT8) and 12 MINBEN capsules (BBAM1 to BBAM12). Table 1 shows the various capsules with the specimens they accommodate and their irradiation conditions.

Table 1. Experimental test matrix

Capsule ID	Material	Condition	Orientation	Specimen type	Specimens	Dose (dpa)	HFIR cycles	Temp (°C)
GAMT1 & GAMT2	LPBF SS-316H (71 J/mm^3)	SR	BD	SS-J3	2	2	1	400
	LPBF SS-316H (71 J/mm^3)	SR	TD		2			
	LPBF SS-316H (52 J/mm^3)	SR	BD		2			
	LPBF SS-316H (52 J/mm^3)	SR	TD		2			
	LPBF SS-316H (71 J/mm^3)	SA	BD		2			
	LPBF SS-316H (71 J/mm^3)	SA	TD		2			
	LPBF SS-316H (52 J/mm^3)	SA	BD		2			
	LPBF SS-316H (52 J/mm^3)	SA	TD		2			
	DED 316L	SR	BD		2			
	DED 316L	SR	TD		2			
	Wrought 316H	SA	RD		2			
	A709	PH	RD		2			
GAMT3 & GAMT4	LPBF SS-316H (71 J/mm^3)	SR	BD	SS-J3	2	10	5	400
	LPBF SS-316H (71 J/mm^3)	SR	TD		2			
	LPBF SS-316H (52 J/mm^3)	SR	BD		2			
	LPBF SS-316H (52 J/mm^3)	SR	TD		2			
	LPBF SS-316H (71 J/mm^3)	SA	BD		2			
	LPBF SS-316H (71 J/mm^3)	SA	TD		2			
	LPBF SS-316H (52 J/mm^3)	SA	BD		2			
	LPBF SS-316H (52 J/mm^3)	SA	TD		2			
	DED 316L	SR	BD		2			
	DED 316L	SR	TD		2			
	Wrought 316H	SA	RD		2			
	A709	PH	RD		2			
GAMT5 & GAMT6	LPBF SS-316H (71 J/mm^3)	SR	BD	SS-J3	2	2	1	600
	LPBF SS-316H (71 J/mm^3)	SR	TD		2			
	LPBF SS-316H (52 J/mm^3)	SR	BD		2			
	LPBF SS-316H (52 J/mm^3)	SR	TD		2			
	LPBF SS-316H (71 J/mm^3)	SA	BD		2			
	LPBF SS-316H (71 J/mm^3)	SA	TD		2			
	LPBF SS-316H (52 J/mm^3)	SA	BD		2			
	LPBF SS-316H (52 J/mm^3)	SA	TD		2			
	DED 316L	SR	BD		2			
	DED 316L	SR	TD		2			
	Wrought 316H	SA	RD		2			
	A709	PH	RD		2			
GAMT7 & GAMT8	LPBF SS-316H (71 J/mm^3)	SR	BD	SS-J3	2	10	5	600
	LPBF SS-316H (71 J/mm^3)	SR	TD		2			
	LPBF SS-316H (52 J/mm^3)	SR	BD		2			
	LPBF SS-316H (52 J/mm^3)	SR	TD		2			
	LPBF SS-316H (71 J/mm^3)	SA	BD		2			
	LPBF SS-316H (71 J/mm^3)	SA	TD		2			
	LPBF SS-316H (52 J/mm^3)	SA	BD		2			
	LPBF SS-316H (52 J/mm^3)	SA	TD		2			
	DED 316L	SR	BD		2			
	DED 316L	SR	TD		2			
	Wrought 316H	SA	RD		2			
	A709	PH	RD		2			

Table 1. Experimental test matrix (continued)

Capsule ID	Material	Condition	Orientation	Specimen type	Specimens	Dose (dpa)	HFIR cycles	Temp (°C)
BBAM 01	LPBF SS-316H (71 J/mm^3)	SR	BD	MBS-1	2	2	1	400
	LPBF SS-316H (71 J/mm^3)	SR	TD		2			
	LPBF SS-316H (52 J/mm^3)	SR	BD		2			
BBAM 02	LPBF SS-316H (52 J/mm^3)	SR	TD	MBS-1	2	2	1	400
	LPBF SS-316H (71 J/mm^3)	SA	BD		2			
	LPBF SS-316H (52 J/mm^3)	SA	BD		2			
BBAM 03	DED 316L	SR	BD	MBS-1	2	2	1	400
	Wrought 316H	SA	RD		2			
	A709	PH	RD		2			
BBAM 04	LPBF SS-316H (71 J/mm^3)	SR	BD	MBS-1	2	10	5	400
	LPBF SS-316H (71 J/mm^3)	SR	TD		2			
	LPBF SS-316H (52 J/mm^3)	SR	BD		2			
BBAM 05	LPBF SS-316H (52 J/mm^3)	SR	TD	MBS-1	2	10	5	400
	LPBF SS-316H (71 J/mm^3)	SA	BD		2			
	LPBF SS-316H (52 J/mm^3)	SA	BD		2			
BBAM 06	DED 316L	SR	BD	MBS-1	2	10	5	400
	Wrought 316H	SA	RD		2			
	A709	PH	RD		2			
BBAM 07	LPBF SS-316H (71 J/mm^3)	SR	BD	MBS-1	2	2	1	600
	LPBF SS-316H (71 J/mm^3)	SR	TD		2			
	LPBF SS-316H (52 J/mm^3)	SR	BD		2			
BBAM 08	LPBF SS-316H (52 J/mm^3)	SR	TD	MBS-1	2	2	1	600
	LPBF SS-316H (71 J/mm^3)	SA	BD		2			
	LPBF SS-316H (52 J/mm^3)	SA	BD		2			
BBAM 09	DED 316L	SR	BD	MBS-1	2	2	1	600
	Wrought 316H	SA	RD		2			
	A709	PH	RD		2			
BBAM 10	LPBF SS-316H (71 J/mm^3)	SR	BD	MBS-1	2	10	5	600
	LPBF SS-316H (71 J/mm^3)	SR	TD		2			
	LPBF SS-316H (52 J/mm^3)	SR	BD		2			
BBAM 11	LPBF SS-316H (52 J/mm^3)	SR	TD	MBS-1	2	10	5	600
	LPBF SS-316H (71 J/mm^3)	SA	BD		2			
	LPBF SS-316H (52 J/mm^3)	SA	BD		2			
BBAM 12	DED 316L	SR	BD	MBS-1	2	10	5	600
	Wrought 316H	SA	RD		2			
	A709	PH	RD		2			

2.3 IRRADIATION HISTORY

All the capsules of this irradiation campaign were successfully assembled and inserted in HFIR's flux trap in target rod rabbit holder positions and started irradiation between cycle 506 and cycle 509. Figure 3 and Figure 4 provide examples of the capsule parts layouts and final assembled capsules. Table 2 summarizes the details of the HFIR cycles related to the capsules of the test matrix in Table 1. Table 3 summarizes the status of the various irradiation capsules. Twelve of the 20 capsules have completed irradiation. Fluence values were calculated from the spatially and temporally dependent HFIR flux integrated over the timeframe of irradiation. Then, the corresponding irradiation dose was calculated using a custom ORNL web-based application [10], which includes this time- and position-resolved fluence data; corresponding SPECTER-based [11, 12] neutron damage calculations are integrated into the user interface. A displacement energy of 40 eV/atom was used for all neutron damage calculations. For future discussions on postirradiation mechanical properties, the two target irradiation temperatures (2 dpa and 10 dpa) will be used as proxies for the more variable rabbit-specific doses estimated in Table 3.

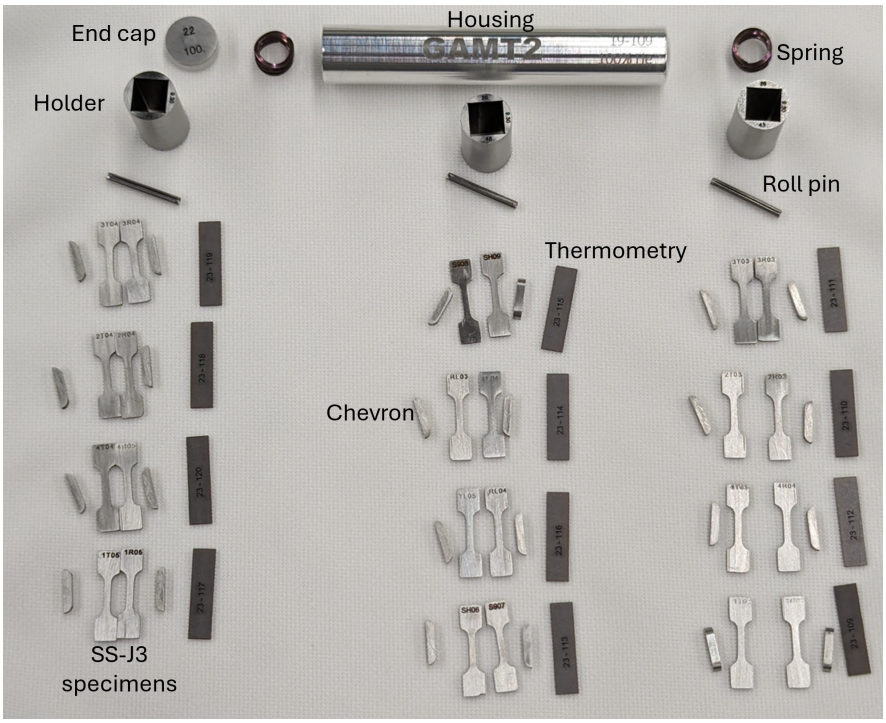

Figure 3. GAMT2 capsule parts layout before capsule assembly.

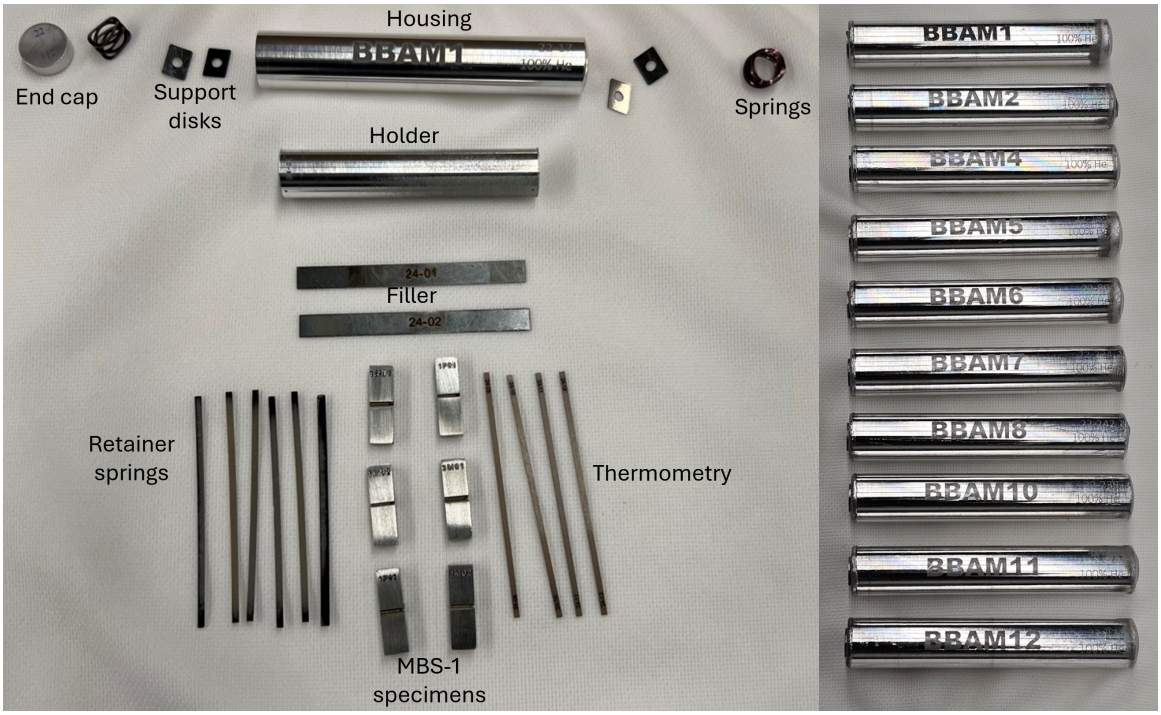

Figure 4. (Left) BBAM1 capsule parts layout before capsule assembly and (right) set of BBAM capsules fully assembled and ready for HFIR insertion.

Table 2. HFIR cycle details

HFIR cycle	Start date	End date	Duration (days)
506	04/09/2024	05/03/2024	24.364
507	06/11/2024	07/05/2024	24.362
508	07/23/2024	08/17/2024	24.710
509	09/03/2024	09/27/2024	24.322
510	10/15/2024	11/08/2024	23.779
*511**	02/18/2025	*03/14/2025**	*23.958**
*512**	*04/08/2025**	*05/02/2025**	*24.000**
*513**	*05/27/2025**	*06/20/2025**	*24.000**

*denotes future projections

Table 3. Irradiation status of the various capsules

Capsule ID	Irradiation location	Start HFIR cycle	End HFIR cycle	Irradiation duration (days)	Thermal fluence <0.4 eV (n/cm^2)	Fast fluence >0.183 MeV (n/cm^2)	Estimated irradiation dose (dpa)	Irradiation status
GAMT1	F4-2	506	506	24.364	5.12E+16	2.44E+16	1.58	Complete
GAMT2	D2-2	506	506	24.364	5.12E+16	2.44E+16	1.58	Complete
GAMT3	C6-2	506	510	121.537	2.55E+17	1.22E+17	8.38	Complete
GAMT4	D6-2	506	510	121.537	2.55E+17	1.22E+17	7.85	Complete
GAMT5	F7-4	506	506	24.364	6.09E+16	2.92E+16	2.06	Complete
GAMT6	C6-5	506	506	24.364	5.85E+16	2.92E+16	1.96	Complete
GAMT7	D6-4	508	512	120.769*	3.02E+17*	1.45E+17*	9.55	On-going
GAMT8	G5-4	509	513	120.059*	3.00E+17*	1.44E+17*	10.15	On-going
BBAM1	E7-3	507	507	24.362	5.85E+16	2.92E+16	1.96	Complete
BBAM2	A2-3	507	507	24.362	5.85E+16	2.92E+16	1.96	Complete
BBAM3	D6-4	506	506	24.364	6.09E+16	2.92E+16	1.93	Complete
BBAM4	E7-5	507	511	121.131*	2.91E+17*	1.45E+17*	9.75	On-going
BBAM5	C6-4	507	511	121.131*	3.03E+17*	1.45E+17*	10.22	On-going
BBAM6	E2-4	507	511	121.131*	3.03E+17*	1.45E+17*	10.23	On-going
BBAM7	D2-5	507	507	24.362	5.85E+16	2.92E+16	1.85	Complete
BBAM8	C2-5	507	507	24.362	5.85E+16	2.92E+16	1.81	Complete
BBAM9	A2-3	506	506	24.364	5.85E+16	2.92E+16	1.96	Complete
BBAM10	E2-3	507	511	121.131*	2.91E+17*	1.45E+17*	9.76	On-going
BBAM11	C6-5	507	511	121.131*	2.91E+17*	1.45E+17*	9.76	On-going
BBAM12	F7-5	507	511	121.131*	2.91E+17*	1.45E+17*	9.77	On-going

*denotes future projections

3. POSTIRRADIATION EXAMINATION OF 2 DPA CAPSULES

3.1 DISASSEMBLY

After HFIR irradiation completion, the 10 low-irradiation-damage capsules (as summarized in Table 1) were transferred to the Irradiated Materials Examination and Testing (IMET) hot cell facility for disassembly. The capsule housing was cut open using a low-speed saw to recover the internal holder(s) and corresponding specimens and thermometry. Figure 5 provides images of the capsule disassembly. All specimens and thermometry were recovered during the disassembly.

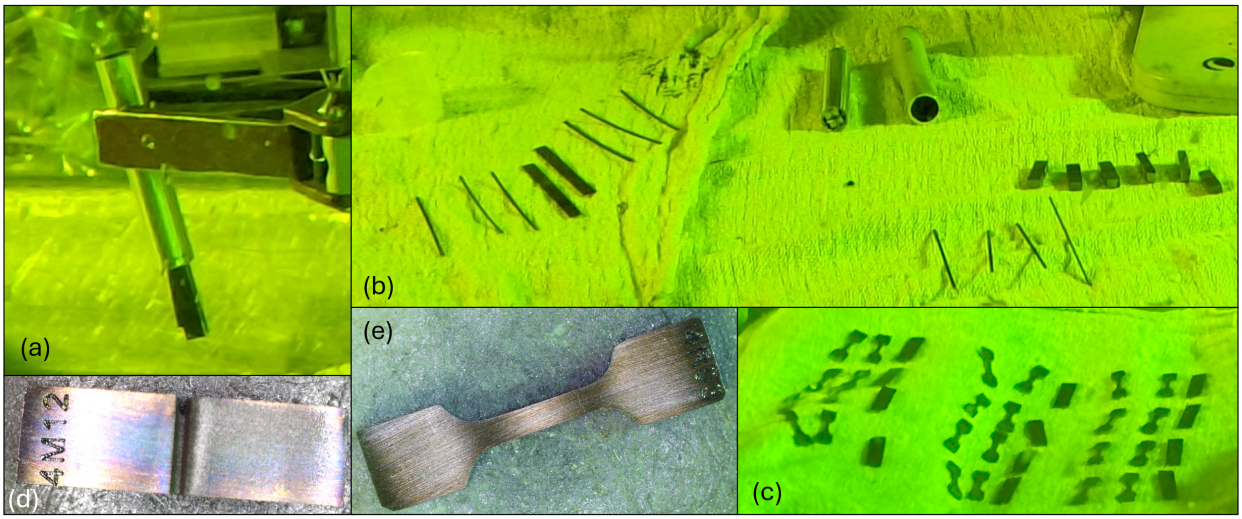

Figure 5. Disassembly pictures. (a) Internal components being slid out of a MINBEN holder, (b) parts layout after disassembly of a MINBEN capsule, (c) SS-J3 tensile specimens and thermometry recovered upon capsule disassembly, (d) MBS-1 specimen recovered during capsule disassembly, and (e) SS-J3 specimen recovered during capsule disassembly.

3.2 THERMOMETRY ANALYSIS

The SiC thermometry recovered during capsule disassembly at IMET was sent to the Low Activation Materials Development and Analysis (LAMDA) laboratory for analysis. The SiC thermometry was analyzed via continuous dilatometry [13] to evaluate the actual experimental temperature. For the GENTEN capsules, half of the thermometry was analyzed to evaluate the experimental temperature. This corresponds to two thermometry per holder (or tier), located on opposite sides of each holder. For the MINBEN capsules, all thermometry was analyzed: each thermometry was cut in half to fit into the dilatometer, and both halves were analyzed. The experimental average specimen temperature was derived from the experimental thermometry temperature measured via dilatometry and from the temperatures of the specimens and thermometry predicted by the numerical analysis. Table 4 presents the results. The experimental temperatures are within 16% of the predicted temperatures. It is important to note that the temperature values in Table 4 represent the average temperature across all thermometry specimens tested within each rabbit. There were cases, however, where there was additional variation within rabbits; therefore, in subsequent plots, the irradiation temperature listed will be provided with even more specificity associated with the average temperature of the thermometry specimens measured within each of the three axial tiers within the GAMT rabbits. This is why some reported temperatures in the plots may be slightly different from the average reported rabbit values in Table 4.

Table 4. Dilatometry results for the 2 dpa capsules

Capsule ID	Target average specimen temp. (°C)	Experimental average specimen temp. (°C) per tier	Experimental average specimen temp. (°C)	Std deviation (°C)	Difference compared with predictions
GAMT1	400	Tier 1 (top): 384 (σ = 19) Tier 2 (middle): 397 (σ = 11) Tier 3 (bottom): 361 (σ = 11)	381	20	−4.8%
GAMT2	400	Tier 1 (top): 413 (σ = 11) Tier 2 (middle): 427 (σ = 34) Tier 3 (bottom): 457 (σ = 9)	432	26	8.0%
GAMT5	600	Tier 1 (top): 576 (σ = 3) Tier 2 (middle): 585 (σ = 10) Tier 3 (bottom): 582 (σ =21)	581	11	−3.2%
GAMT6	600	Tier 1 (top): 526 (σ = 4) Tier 2 (middle): 518 (σ = 4) Tier 3 (bottom): 582 (σ = 18)_	518	11	−13.7%
BBAM1	400	N/A	349	11	−12.8%
BBAM2	400	N/A	346	19	−13.6%
BBAM3	400	N/A	363	14	−9.2%
BBAM7	600	N/A	505	24	−15.9%
BBAM8	600	N/A	504	29	−16.1%
BBAM9	600	N/A	522	25	−12.9%

3.3 TENSILE TESTING

Unirradiated mechanical testing was performed out of cell using an Instron Model 5900R double-column electromechanical frame coupled with a custom induction heating setup to enable high-temperature mechanical testing in an air atmosphere. Testing was performed on unirradiated SS-J3 samples at a strain rate of 10^{-3} s^{-1} using shoulder loading. The tensile frame used for the irradiated specimens in this study was an Instron Model 5967 double-column electromechanical frame coupled with a custom-built Oxy-Gon high-temperature vacuum furnace. The tensile frame has a calibrated 5 kN load cell, and tensile testing was performed using a strain rate of 10^{-3} s^{-1}, which was conducted and measured using crosshead displacement because of the small sample size. The test matrix included four SS-J3-style tensile specimens for each material-irradiation condition, two of which were slated for testing at room temperature (23°C) and two of which were slated for testing at the target irradiation temperature (either 400°C or 600°C, respectively). However, as the thermometry results in Table 4 illustrate, although the irradiation temperature was near the target temperature for the lower-temperature case, one of the elevated temperature tensile rabbits (GAMT6) deviated from the target temperature by 82°C. Thus, for room temperature measurements, at least two specimens were tested per condition. However, for capsules with a target irradiation temperature of 600°C, one specimen (from GAMT5) was tested at 600°C, and another specimen (from GAMT6) was tested at 500°C to ensure that the test temperature more realistically represented conditions near the measured irradiation conditions. All irradiated tensile testing at elevated temperature was conducted in vacuum, whereas room temperature testing was conducted in air.

Time, crosshead displacement, load, and gauge cross section dimensions were recorded for all tests. Because strain was not measured directly and was computed based on crosshead displacement, a compliance correction method was employed so that the approximate plastic strain values could be extracted from the crosshead displacement data.

$$\varepsilon_p = \frac{\delta - P \times C_{LL}}{l} \qquad \text{Eq. (1)}$$

In Eq. (1), ε_p is the plastic strain; δ and P are the crosshead displacement and load, respectively; C_{LL} is the load line compliance calculated as the inverse of the elastic slope of the raw load–displacement curve; and l is the gauge length. When the load–displacement curve is converted to a stress–plastic strain curve, the pertinent tensile values can be calculated. The 0.2% offset yield strength (YS) is the stress at 0.2% plastic strain, the ultimate tensile strength (UTS) is the maximum stress, the uniform elongation (UE) is the plastic strain value corresponding to the UTS, and the total elongation (TE) is the plastic elongation at failure.

Over the course of this low-dose testing campaign, more than 150 tensile tests have been conducted, and the data are too numerous to show every individual tensile curve; however, the individual tensile tests will be made available upon request. In lieu of showing the compliance-corrected stress vs. strain curves for all samples, selected room temperature and elevated temperature tests are shown to provide context for the types of irradiation-induced mechanical property changes that are being observed generally for the LPBF materials.

In Figure 6, room temperature tests are shown for unirradiated (black) specimens of ORNL-optimized LPBF SS-316H. This build, named Tensile Blocks 01 and having a set of processing parameters equating to a VED of 71 J/mm^3, represents the printing condition that to date has shown the highest creep strength and creep life of the various builds investigated out of pile. The colored lines indicate room temperature tests conducted on irradiated samples following irradiation to the target damage level of 2 dpa. The color of each curve indicates the average tensile specimen irradiation temperature for the tier of the capsule corresponding to the tested specimen (from Table 4)

Before irradiation, the BD, owing to the preferential grain orientation in that direction and the slightly elongated grain morphology in that orientation, provides the easiest dislocation slip pathway during deformation. This results in a lower YS (approximately 305 MPa) in the BD vs. the 339 MPa YS in the TD. Following irradiation at the lower target irradiation temperature of 400°C (the two rabbits hit tier temperatures for these specimens of 384°C and 413°C), the YS is increased by at least 100 MPa for each of these conditions. In the BD, the lowest-temperature irradiation had the highest increase in YS, and both lower irradiation temperatures resulted in similar hardening behavior in the TD. At the higher measured irradiation temperatures (526°C and 576°C), either no hardening or some softening occurred vs. the unirradiated strength. However, for all samples, regardless of irradiation temperature, the strain hardening rate increased (concurrent with an increased total UTS), and all samples (both build and transverse orientations) decreased in ductility measured via both UE and TE.

Elevated temperature results for the same Tensile Blocks 01 build (in both the stress-relieved and solution-annealed conditions) are shown in Figure 7. Because the elevated temperature properties are the most important for advanced reactor operating conditions (>400°C), the samples irradiated and tested at the highest irradiation temperature (approximately 600°C) are presented to show the general trends for the LPBF material performance. Figure 7 shows fundamentally different performance between the stress-relieved and solution-annealed variants. For instance, in the unirradiated condition, both orientations of the stress-relieved materials had less than 10% UE (strain hardening capacity) vs. the solution-annealed condition, which consistently measured between 20% and 30% UE depending on test orientation. This finding agrees with what was recently noted for low-creep ductility observed in the stress-relieved material vs. the solution-annealed material in out-of-pile tests [6].

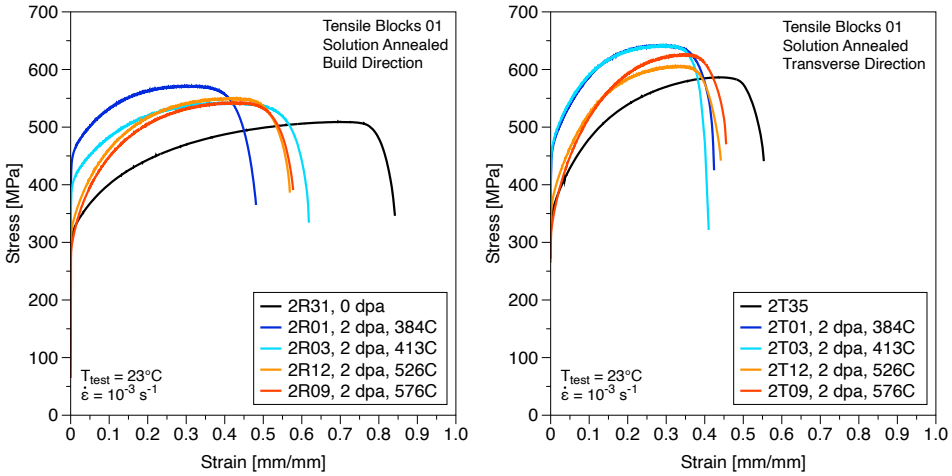

Figure 6. Room temperature compliance-corrected engineering stress vs. plastic strain curves for LPBF SS-316H irradiated to 2 dpa in HFIR as a function of measured irradiation temperature. The left image provides data with the loading axis aligned in the BD, and the right image correlates to specimens aligned in the TD. Irradiation temperatures represent the average of at least two SiC thermometry specimens within the section of the rabbit closest to the test specimen of interest.

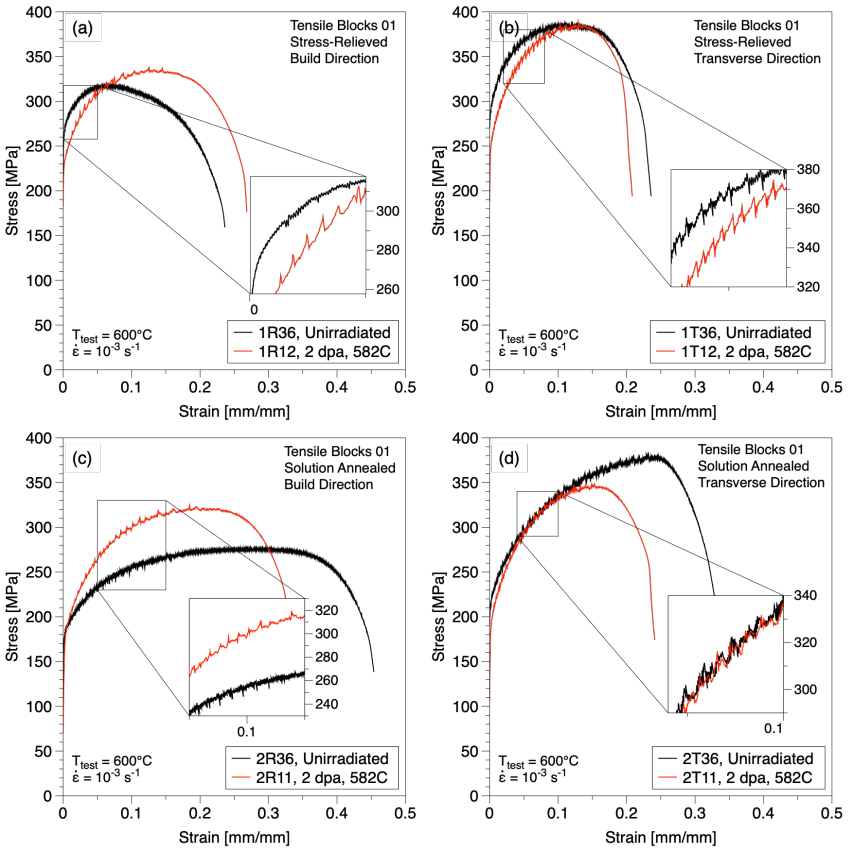

Figure 7. Elevated temperature engineering stress vs. plastic strain curves for Concept Laser build Tensile Blocks 01 in the (top left and right) stress-relieved and (bottom left and right) solution-annealed conditions following irradiation to 2 dpa at a target testing and irradiation temperature of 600°C. For each heat treatment condition, the top and bottom left plots indicate testing aligned with the BD, and the top and bottom right plots are aligned in the TD.

Interestingly, the postirradiation properties trend toward similar values of strength and ductility, irrespective of initial heat treatment. For example, the stress-relieved sample tested in the BD actually demonstrated some toughening (increase in both UTS and UE) following irradiation, whereas the TD showed little change in the heat treatment condition. In the solution-annealed condition, the YS was largely unchanged, but the higher ductility deteriorated more significantly following irradiation in comparison with the stress-relieved condition. In the solution-annealed BD specifically, the total strength increased, but the ductility decreased by over 10% relative to the unirradiated condition. Because of the already high strain hardening rate of the TD in the same heat treatment condition, only a decrease in UTS, UE, and TE was observed. In short, the margin of TE in the BD (SA/SR) decreased from 1.92 to 1.22 following only 2 dpa of irradiation.

For all the elevated temperature test conditions, the stress/strain curves from afar all seem to be less smooth in comparison to the curves of tests at room temperature. This noisy appearance is not due to any load cell–related signal-to-noise issues but instead stems from what appears to be dynamic strain aging, which is becoming apparent in these materials at the elevated temperature testing condition. In the stress-relieved condition tested parallel to the BD (Figure 7a), the magnitude and frequency of the dynamic strain aging serrations is smallest, but it is observable in all cases. Because of the relation of this type of serrated flow with the distribution of interstitial elements within the microstructure, future work should be conducted on irradiated specimens to reveal the spatial distribution of elements within grains and along grain boundaries vs. their unirradiated counterparts as a recommended FY 2026 activity.

Figure 8, Figure 9, and Figure 10 provide a summary of the metadata (YS, UTS, UE, and TE) for various builds and heat treatment conditions. Figure 8 focuses on the differences between the properties of Tensile Blocks 01 (VED = 71 J/mm^3) and Tensile Blocks 02 (VED = 52 J/mm^3) in the stress-relieved condition before and after irradiation. Figure 9 summarizes data for the two builds in the solution-annealed condition. Finally, Figure 10 shows a comparison between the wrought 316H and precipitation-hardened A709 materials. The open squares in all three figures indicate the tensile tests in the unirradiated conditions, and the closed circles indicate tests performed on irradiated specimens (colored with respect to the measured irradiation temperatures).

In the stress-relieved builds, although irradiation-induced hardening was observed at room temperature for specimens irradiated near 400°C, appreciable hardening seemed to occur at the 400°C test condition only if the irradiation temperature undershot the target temperature. Otherwise, for the higher-temperature irradiation and test conditions (500–600°C), the as-irradiated strength and ductility of the stress-relieved samples were similar to those of the unirradiated condition (regardless of test orientation). For the solution-annealed samples, the extent of the irradiation hardening at room temperature (the change in YS) was similar to that measured for the stress-relieved samples. However, more significant changes in strength and ductility were observed at elevated temperature than the stress-relieved condition. For instance, at all test temperatures, there was a decrease in both UE and TE, irrespective of irradiation/test temperature. Similar to the stress-relieved condition, there was not a noticeable change in strength (either YS or UTS) at the higher test temperatures (400°C–600°C) when the target irradiation temperature was greater than 400°C.

The wrought material generally outperformed the LPBF material in terms of total ductility at both room temperature and elevated temperature following irradiation. The wrought SS-316H material did not decrease in ductility following elevated temperature irradiation, as shown in Figure 10, even with comparable strength values following irradiation. For comparison, the higher-nickel-content wrought A709 alloy showed considerable ductility degradation at all irradiation temperatures. Additional work will be undertaken in the future to perform detailed postirradiation examination on these alloys.

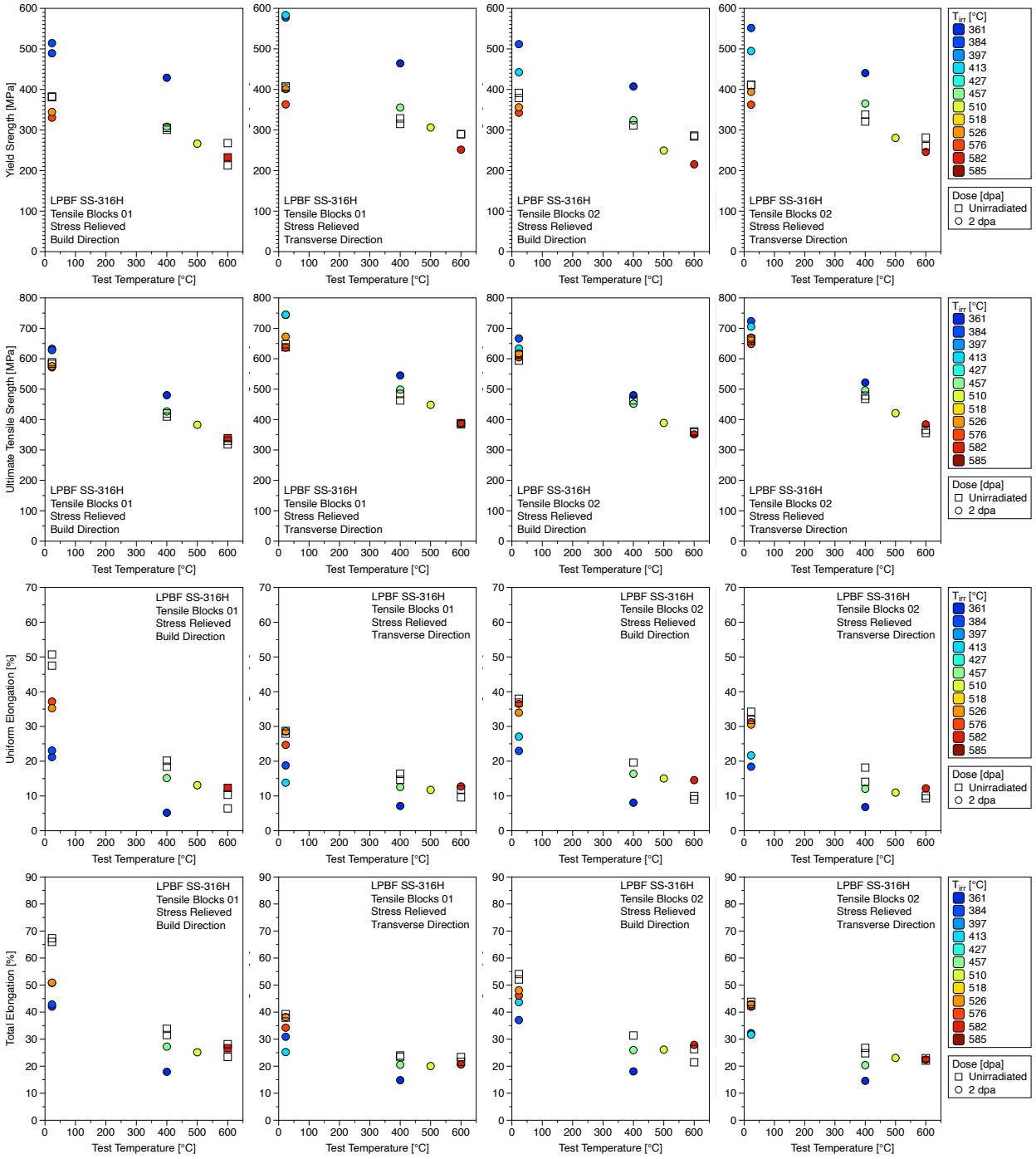

Figure 8. Comparison of YS, UTS, UE, and TE values as a function of test temperature and irradiation temperature for stress-relieved LPBF SS-316H samples in the Tensile Blocks 01 and Tensile Blocks 02 builds in the build and transverse orientations. Open squares indicate the results of pre-irradiation tests, whereas filled-in circles represent irradiated specimens. Colors correspond to the right-hand color bars.

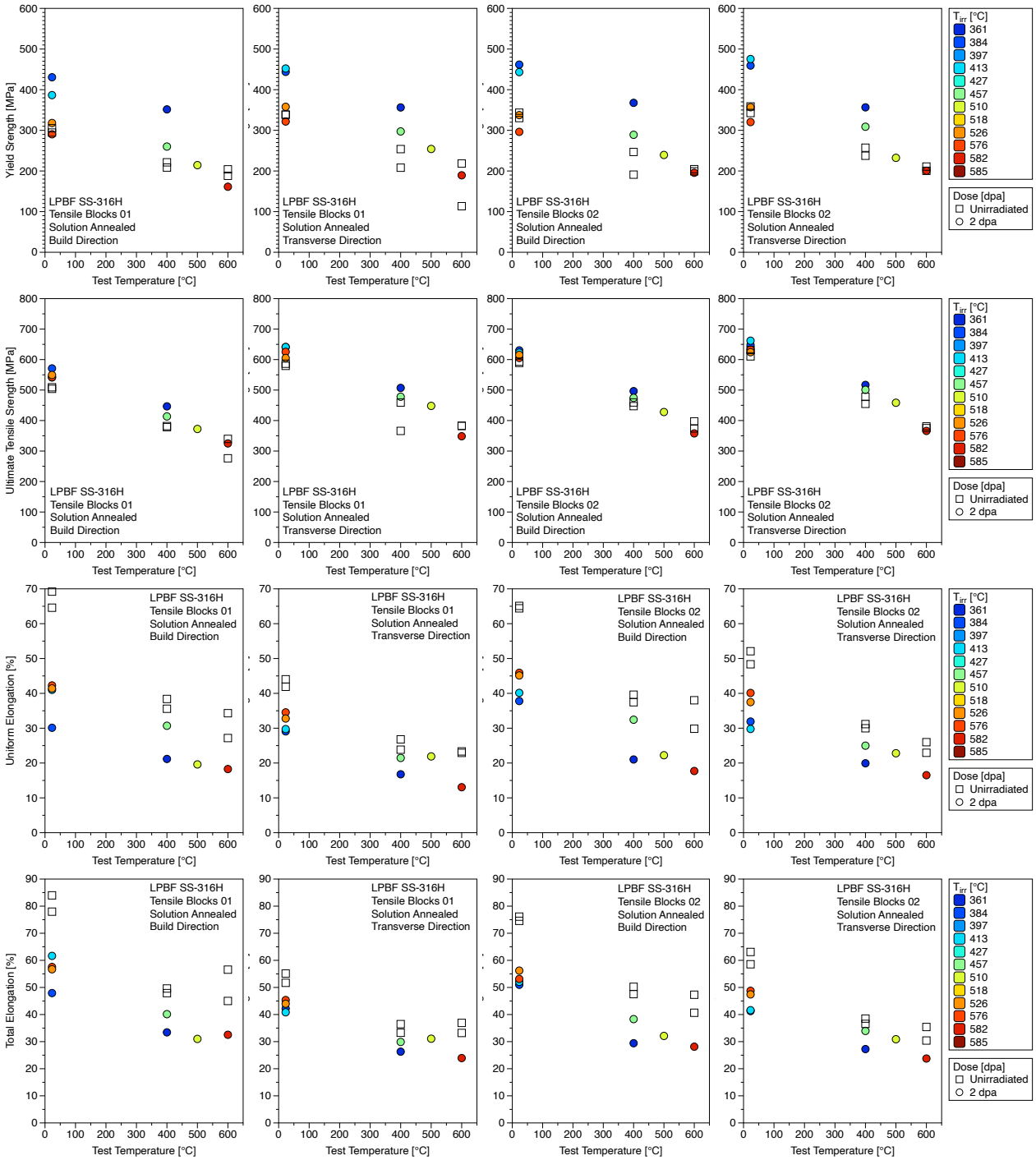

Figure 9. Comparison of YS, UTS, UE, and TE values as a function of test temperature and irradiation temperature for solution-annealed LPBF SS-316H samples in the Tensile Blocks 01 and Tensile Blocks 02 builds in the build and transverse orientations. Open squares indicate the results of pre-irradiation tests, whereas filled-in circles represent irradiated specimens. Colors corresponding to the right-hand color bars.

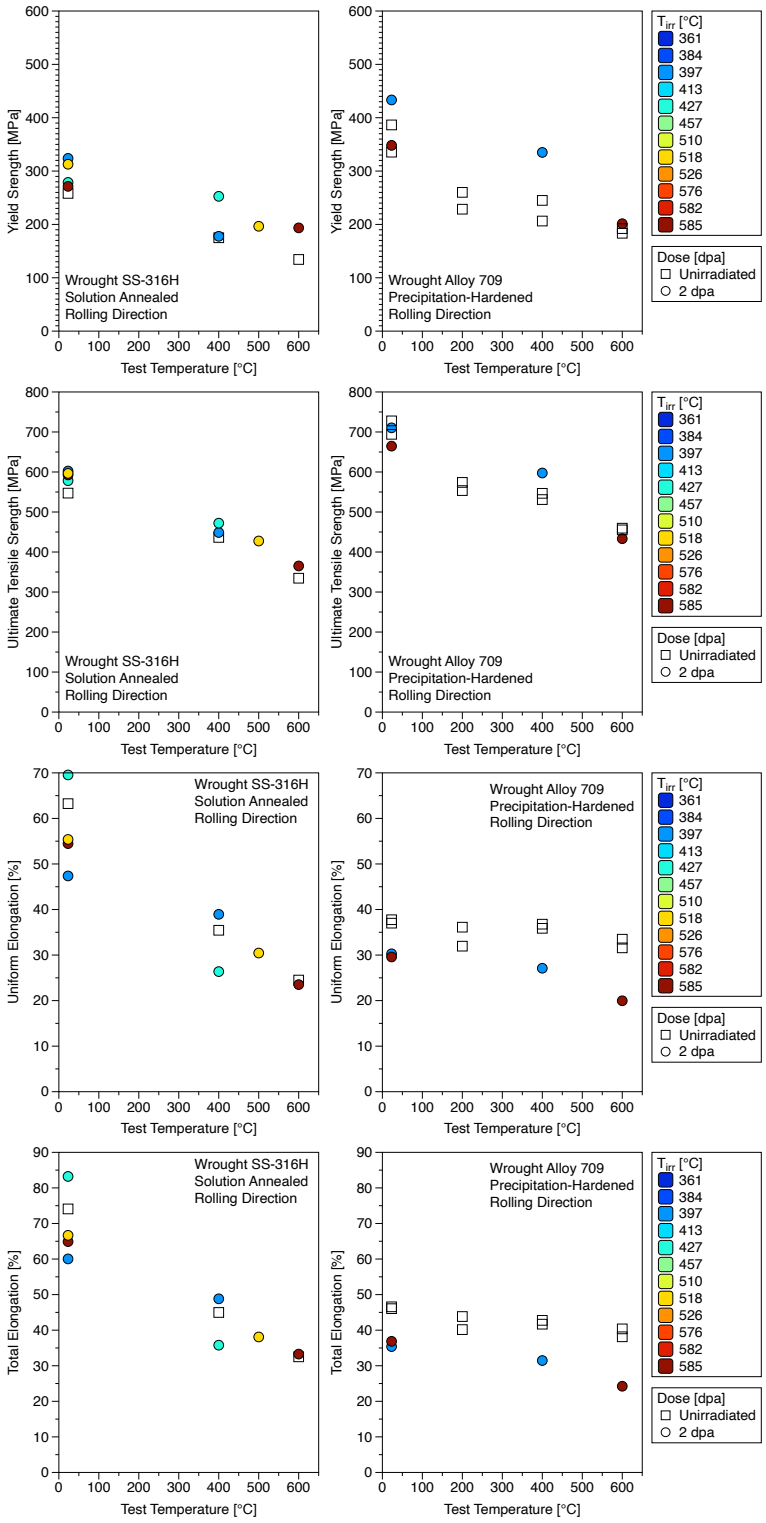

Figure 10. Comparison of YS, UTS, UE, and TE values as a function of test temperature and irradiation temperature for solution-annealed wrought SS-316H and precipitation-hardened A709 in the rolling direction. Open squares indicate the results of pre-irradiation tests, whereas filled-in circles represent irradiated specimens. Colors correspond to the right-hand color bars.

To compare the various builds and heat treatments, room temperature data and the tensile tests performed at 600°C are replotted in Figure 11 to show the relative performance following irradiation to 2 dpa at the same irradiation target temperature. At the elevated temperature testing condition, the stress-relieved builds (both VED parameter sets) consistently have the lowest ductility performance relative to the other tested materials. Similarly, the wrought SS-316H consistently has the highest ductility amongst all material permutations. As expected, the precipitation-hardened A709 has the highest UTS, but the stress-relieved variants of LPBF SS-316H are competitive even with their concurrently low postirradiation ductility.

Of particular interest in this comparison is the relative similarity in postirradiation tensile strength/ductility between the two different builds (Tensile Blocks 01 and Tensile Blocks 02). As mentioned previously, the Tensile Blocks 01 build, when creep-tested out of pile at 725°C and 100MPa, had double the creep life with a much lower secondary creep rate in comparison with the Tensile Blocks 02 build [6]. The differences between the microstructures are slight, with each having a similar grain size distribution, but with the second (lower VED) build having about 0.3% total porosity, which could have been a factor in its premature failure. However, as shown in the previous figures as well as in the direct comparison of postirradiation behavior here, there are minimal differences in the time-independent properties of these two builds following irradiation. Both builds have greater than 20% TE following 2 dpa irradiation at 600°C, and the strength values are within the 10% margin of error expected from the statistics associated with tensile test data variance.

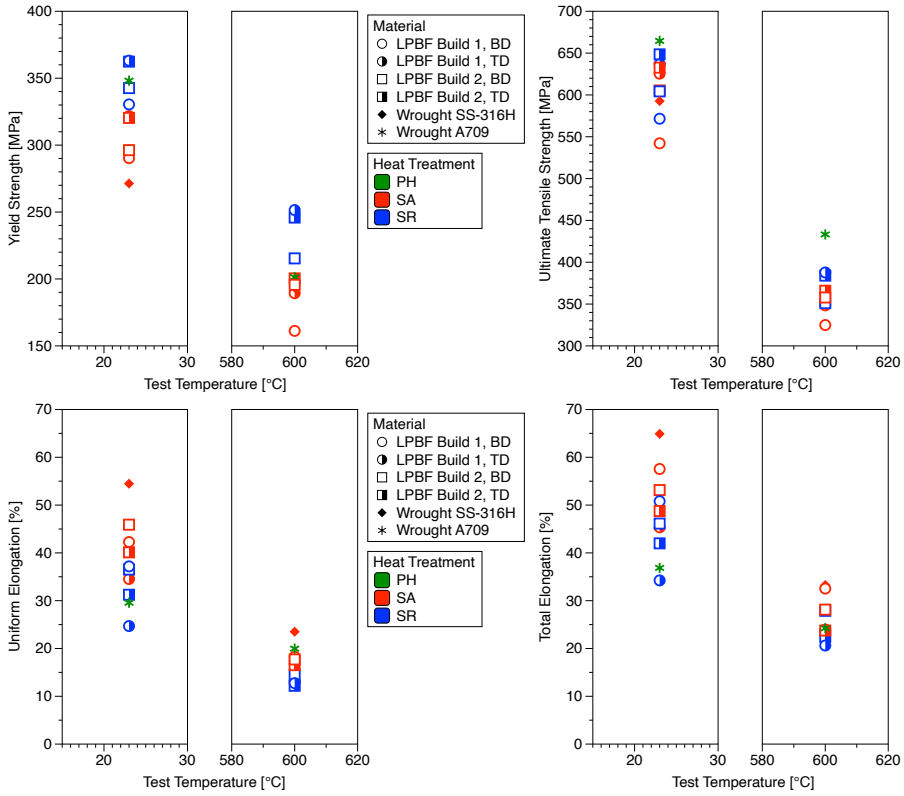

Figure 11. Comparison of YS, UTS, UE, and TE for the wrought (SS-316H and A709) and LPBF SS-316H alloys included in this irradiation campaign following irradiation at a target temperature of 600°C. The colors of each datapoint represent the precipitation-hardened (green), solution-annealed (red), and stress-relieved (blue) conditions, respectively, and the marker style is associated with the material type and test orientation.

3.4 FRACTURE TOUGHNESS TESTING

In addition to tensile testing, J–R fracture testing of MBS-1 specimens was performed. The initial fatigue precracking step was performed on one of two TestResources servoelectric mechanical test frames. Precracking consisted of loading the specimens in a 13 mm span three-point bend from a minimum load of 50 N to a maximum load of 650–800 N at 15 Hz; because of machining inconsistencies of the specimen starter notches, the maximum load varied to compensate. The specimen was loaded cyclically with the intent of achieving the desired precrack length of approximately half the specimen thickness ($W/2$) in 30,000–50,000 cycles. Because of the extremely small specimen geometry, a gauge-free precracking method had to be employed; rather than monitoring crack growth directly, changes in displacement during cyclic loading were correlated to changes in crack length. Because the specimen starter notches were often much shorter than nominal, it was determined that a change in peak displacement of 25–30 μm after an initial "breaking in" period of 3,000–10,000 cycles was necessary to achieve an acceptable precrack length. Once the desired change in peak displacement was achieved, the maximum load was reduced such that the load amplitude was half that of the initial precracking step. An additional 10,000 cycles were then applied to sharpen the crack tip, ensuring maximum stress concentration.

After irradiation, monotonic J–R testing was performed in a hot cell setting under ambient conditions using an MTS servohydraulic test frame. An initial preload of approximately 20 N was applied to maintain load train tension while correct fixture and specimen seating were ensured. After correct fixture/specimen seating was confirmed, quasi-static testing was performed in displacement control at 0.005 mm/s until either the load dropped to approximately half the maximum load or an excessive displacement (4–5 mm) was reached. Time, load, and displacement data were acquired at a rate of 10 Hz. To mark the final crack length, specimens were heat-tinted by placing them on a hot plate at 450°C for up to 10 min or until a color change in the crack surface was confirmed. This process resulted in a color change related to the formation of a nanoscale oxide layer on the pre-test crack, differentiating this pre-existing crack surface from the new surface revealed after testing. The specimens were then re-inserted into the fixture and frame where the samples were fully broken in half.

After final specimen breakage, one fracture surface of each specimen was imaged (example shown in Figure 12), and the initial and final crack lengths were measured using a nine-point weighted average in accordance with ASTM E1820. Fracture lengths were measured in pixels and then converted to millimeters using the undeformed bottom edge (width) as a scale, which was assumed to be nominal, as was the specimen thickness. However, because of machining inconsistencies, specimen side grooves were also measured using a similar method rather than being assumed to be nominal. With the raw load–displacement data and crack geometry data obtained, the fracture resistance or J–R curve of each specimen could be constructed. Given the lack of direct crack opening measurement, the only useable calculation method was the normalization method outlined in Byun et al. [14]. A modified normalization method was used for this test campaign because it was found that direct application of the normalization method led to significant calculation errors owing to high material ductility and very small specimen size. Although this modified method allowed for sensible J–R data to be produced, given the combined high material ductility and small specimen geometry (which do not allow for plane strain conditions), as well as the deviation from the ASTM E1820 method, the fracture results reported should not be used as a design basis. However, the modified normalization method has been shown to be effective as a screening tool and for showcasing the effects of differences in processing and environmental conditions on fracture behavior.

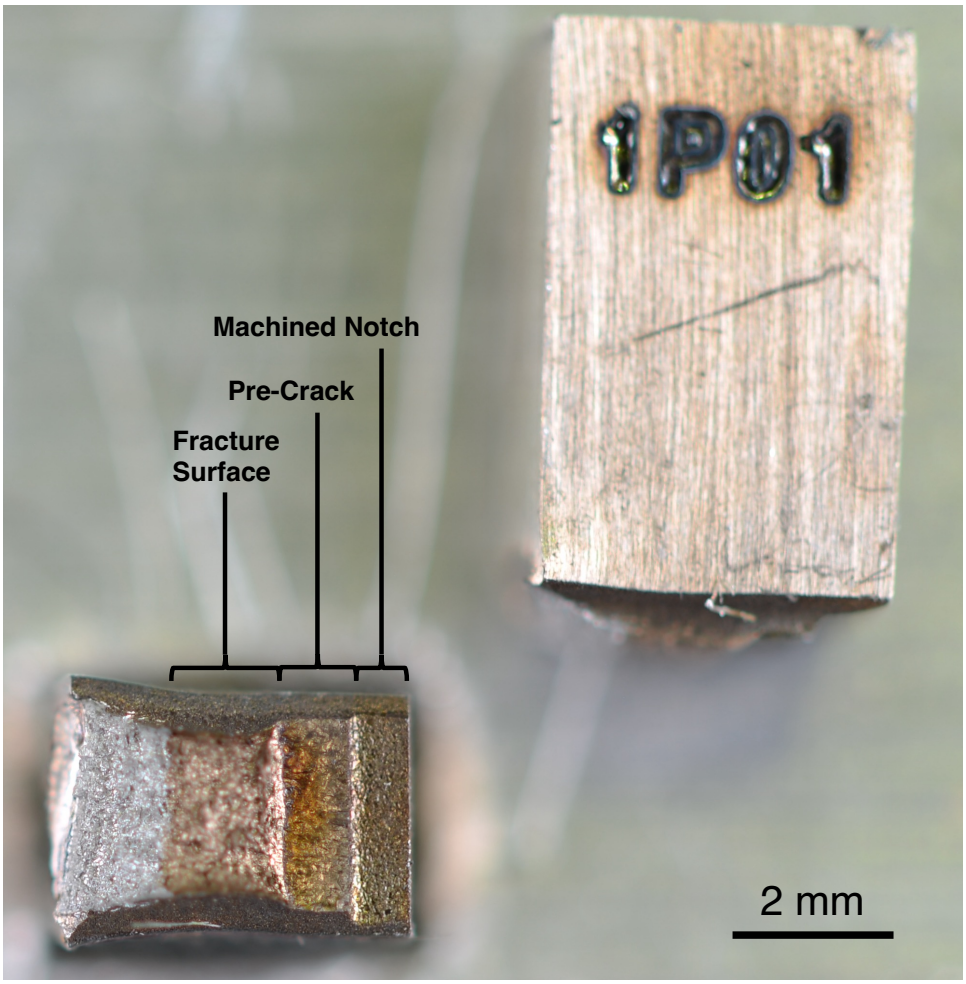

Figure 12. Example of a tested MBS-1 specimen with labeled characteristic regions along the fracture surface.

Once the J–R curve was constructed, such as the one shown in Figure 13, the 0.1 and 0.2 mm offset *J* and *K* values could be determined.

$$K_{0.1,0.2\,mm} = \left(J_{0.1,0.2mm}\, x \frac{E}{1-\nu^2}\right)^{0.5} \qquad \text{Eq. (2)}$$

In Eq. (2), $J_{0.1,\,0.2\,\text{mm}}$ are the *J* values at either the 0.1 or 0.2 mm offset intercept, *E* is the elastic modulus, and *v* is Poisson's ratio. Although Eq. (2) assumes plane strain conditions, plane strain is, in actuality, unlikely to have been achieved at any condition because of the small specimen geometry and high ductility of SS-316H. In this work, $K_{0.2\text{mm}}$ is the preferred parameter to report over $K_{0.1\text{mm}}$ because it has been generally found to show less scattering and is therefore better suited for showcasing material evolution with irradiation.

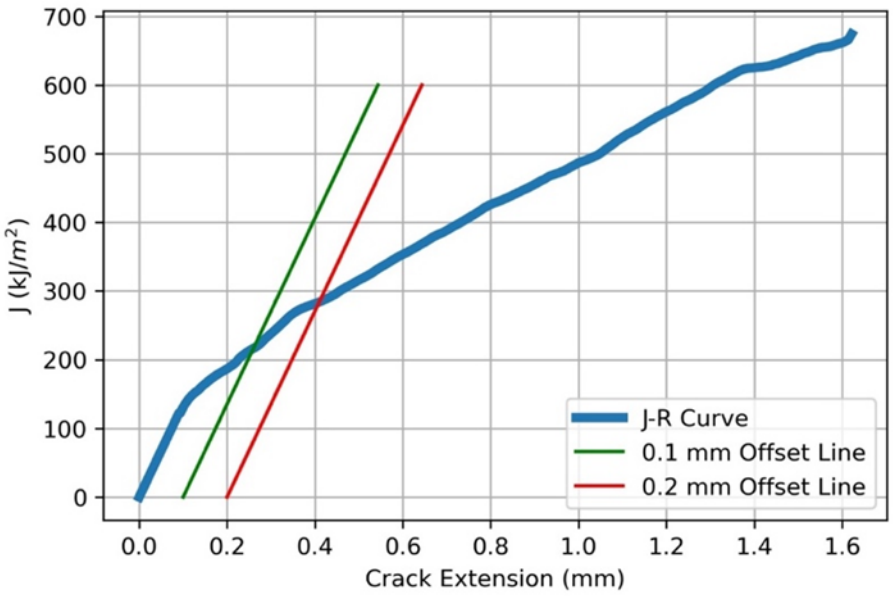

Figure 13. Example J–R curve showing the 0.1 and 0.2 mm offset lines. The offset line slopes are the same as the slope of the blunting region of the J–R curve.

The J–R fracture results reported as $K_{0.2mm}$ are shown in Figure 14. For the wrought 316H, although both irradiation conditions show good toughness, there is a significant decrease in both cases compared with the unirradiated condition. The 400°C target/363°C actual specimen shows a decrease of approximately 170 MPa√m relative to the unirradiated condition, and the decrease of the 600°C target/522°C actual specimen is even greater (approximately 240 MPa√m). For the LPBF SS-316H materials, at the 600°C target/approximately 500°C actual irradiation condition (except for the solution-annealed 52 J/mm^3 material), all other materials show toughness comparable with that of their unirradiated counterparts, with several demonstrating a modest increase in toughness; the noticeable decrease in toughness for the 52 J/mm^3 solution-annealed material requires additional investigation to determine its source. For the 400°C target/approximately 350°C actual materials, a decrease in toughness relative to their unirradiated counterparts is observed for all specimens. However, good toughness retention overall is demonstrated, with the greatest reduction being only 47 MPa√m, or approximately 16% of baseline. Structurally, all materials show acceptable fracture resistance at all conditions, though the solution-annealed LPBF SS-316H at 2 dpa/approximately 500°C should be investigated further to determine if its more significant fracture toughness reduction is systemic or simply isolated to that particular specimen.

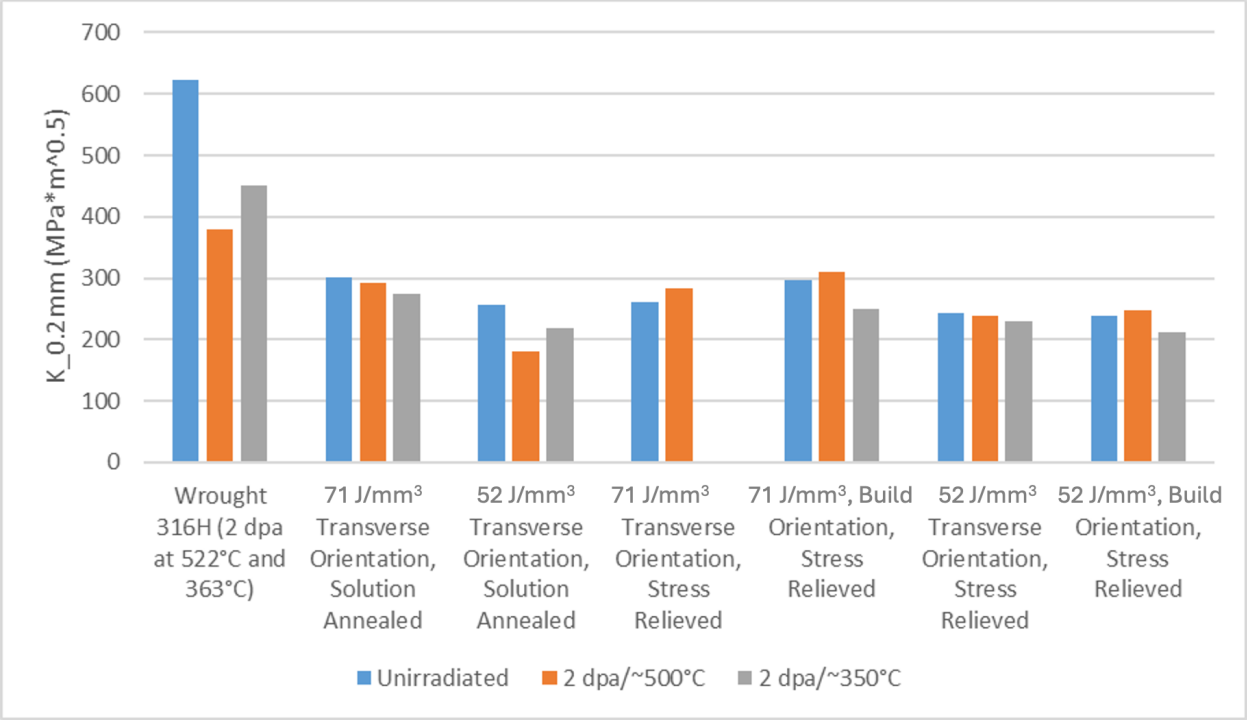

Figure 14. $K_{0.2mm}$ values for the 2 dpa irradiated wrought and AM 316H materials tested at room temperature.

4. CONCLUSIONS

This report summarizes the preliminary tensile and fracture toughness data collected to date on wrought alloys (SS-316H and A709) relative to newly produced LPBF SS-316H material with two representative postbuild heat treatments. Following irradiation to 2 dpa at 400°C, some irradiation hardening was observed for all materials investigated when tested at room temperature, and changes in strength were minimal when evaluated at elevated temperature. At the higher-temperature irradiation condition, no significant changes to elevated temperature strength were noted, but significant decreases in ductility were observed for the solution-annealed LPBF SS-316H material, resulting in similar levels of postirradiation ductility between stress-relieved and solution-annealed variants. Although the tensile properties of the wrought SS-316H material did not deteriorate following irradiation, the fracture toughness of the material decreased more significantly than that of the LPBF SS-316H materials; however, the total fracture toughness remained higher than that of the additively manufactured parts. Future work is ongoing to identify the root cause of these changes in mechanical performance following irradiation.

ACKNOWLEDGMENTS

The authors would like to acknowledge the contributions of the dedicated personnel at Oak Ridge National Laboratory's IMET facility, including Clay Morris and Jerid Metcalf. Additionally, the team would like to thank the members of the LAMDA laboratory—namely, Patricia Tedder and Stephanie Curlin—for facilitating sample receipt, inventory, and eventual measurements of SiC thermometry specimens for the project. This irradiation would not have been possible without the assistance of Abby Till and Trevor Parker from the Irradiation Engineering Group.

5. REFERENCES

[1] J. Clayton, D. Millington-Smith, B. Armstrong, The application of powder rheology in additive manufacturing, Jom 67(3) (2015) 544-548.
[2] Z. Wang, C. Jiang, P. Liu, W. Yang, Y. Zhao, M.F. Horstemeyer, L.-Q. Chen, Z. Hu, L. Chen, Uncertainty quantification and reduction in metal additive manufacturing, Npj Computational Materials 6(1) (2020) 175.
[3] P. Nandwana, A. Plotkowski, R. Kannan, S. Yoder, R. Dehoff, Predicting geometric influences in metal additive manufacturing, Materials Today Communications 25 (2020) 101174.
[4] I.F. Ituarte, E. Coatanea, M. Salmi, J. Tuomi, J. Partanen, Additive manufacturing in production: a study case applying technical requirements, Physics Procedia 78 (2015) 357-366.
[5] C. Massey, P. Nandwana, H. Hyer, S. Nayir, J. Kendall, C. Joslin, R. Duncan, D. Collins, T. Graening, F.L. III, L. Scime, Z. Snow, A. Ziabari, T. Butcher, R. Dehoff, Data-Driven Optimization of the Processing Window for 316H Components Fabricated Using Laser Powder Bed Fusion, Oak Ridge National Laboratory, 2023, pp. 1-44.
[6] Y.C. Xuan Zhang, Srinivas Aditya Mantri, Lin Gao, Edward Listwan, Joe Listwan, Michael McMurtrey, Ninad Mohale, Caleb Massey, FY24 Integrated Results for High-Temperature Mechanical Testing of LPBF 316H Stainless Steel., Argonne National Laboratory, pp. 1-61.
[7] P. Champlin, J. Burns, C.M. Petrie, X. Hu, K.D. Linton, R.H. Howard, K.A. Terrani, Capsule and Specimen Geometries for HFIR Irradiation Testing Supporting the Transformational Challenge Reactor, Oak Ridge National Lab.(ORNL), Oak Ridge, TN (United States), 2019.
[8] P. Champlin, C. Massey, A. Le Coq, S. Taller, T. Byun, K. Linton, AMMT FY23 HFIR Irradiation Test Matrix–Supported by the Design of a Miniature Bend Bar Irradiation Vehicle, Oak Ridge National Laboratory (ORNL), Oak Ridge, TN (United States), 2023.
[9] T. Allen, F. Balbaud-Celerier, T. Asayama, M. Pouchon, J. Busby, S. Maloy, J. Park, C. Fazio, Y. Dai, P. Agostini, Status report on structural materials for advanced nuclear systems, Organisation for Economic Co-Operation and Development, 2013.
[10] J. Burns, K. Terrani, A web-based application for standardization of radiation damage calculations, Oak Ridge National Laboratory (ORNL), Oak Ridge, TN (United States), 2018.
[11] L.R. Greenwood, R.K. Smither, SPECTER: neutron damage calculations for materials irradiations, Argonne National Lab.(ANL), Argonne, IL (United States), 1985.
[12] M. Norgett, M. Robinson, I.M. Torrens, A proposed method of calculating displacement dose rates, Nuclear engineering and design 33(1) (1975) 50-54.
[13] A.A. Campbell, W.D. Porter, Y. Katoh, L.L. Snead, Method for analyzing passive silicon carbide thermometry with a continuous dilatometer to determine irradiation temperature, Nuclear Instruments and Methods in Physics Research Section B: Beam Interactions with Materials and Atoms 370 (2016) 49-58.
[14] T. Byun, S. Maloy, J. Yoon, Small specimen reuse technique to evaluate fracture toughness of high dose HT9 steel, Sixth International Symposium on Small Specimen Test Techniques, ASTM International, 2014, pp. 1-22.